

## Quasielastic ( $p, n$ ) reactions induced by polarized protons

J. Gosset, B. Mayer, and J. L. Escudé

*Service de Physique Nucleaire a Moyenne Energie, Centre d'Etudes Nucléaires de Saclay, BP. 2, 91190 Gif-sur-Yvette, France*

(Received 12 November 1975)

The differential analyzing power has been measured in the quasielastic ( $p, n$ ) reaction on  $^{49}\text{Ti}$ ,  $^{56}\text{Fe}$ ,  $^{64}\text{Ni}$ ,  $^{70}\text{Zn}$ ,  $^{90}\text{Zr}$ ,  $^{96}\text{Zr}$ ,  $^{117}\text{Sn}$ ,  $^{165}\text{Ho}$ , and  $^{208}\text{Pb}$  at 22.8 MeV. Fits to the experimental data in a macroscopic Lane-model analysis were improved by adding a spin-orbit term  $V_{so}^{(1)}$  in the isospin-dependent part of the optical potential. The sign of  $V_{so}^{(1)}$  agrees with that given by a simple model and its value does not depend very much on the target nucleus. However, the average value of  $V_{so}^{(1)}$  depends on the geometry used for the spin-orbit optical potential, an ambiguity which corresponds to a nearly constant product of the depth and of the diffuseness. A microscopic distorted-wave Born-approximation analysis was made, but due to several ambiguities in the calculation, it has not been possible to determine the isovector spin-orbit part  $v_{LS\tau}$  of the nucleon-nucleon effective interaction.

NUCLEAR REACTIONS Quasielastic ( $\vec{p}, n$ ) reactions on  $^{49}\text{Ti}$ ,  $^{56}\text{Fe}$ ,  $^{64}\text{Ni}$ ,  $^{70}\text{Zn}$ ,  $^{90}\text{Zr}$ ,  $^{96}\text{Zr}$ ,  $^{117}\text{Sn}$ ,  $^{165}\text{Ho}$ , and  $^{208}\text{Pb}$ ;  $E = 22.8$  MeV; measured differential analyzing power  $A(\theta)$ ; macroscopic Lane-model analysis with an isospin-dependent spin-orbit term in the optical potential; microscopic DWBA analysis.

### I. INTRODUCTION

Quasielastic (QE) ( $p, n$ ) reactions, i.e. ( $p, n$ ) reactions leaving the residual nucleus in the analog of the target ground state, have proved to be a very powerful tool to study the isospin dependence of the nucleon-nucleus optical potential<sup>1</sup> within the framework of the Lane model.<sup>2</sup> Recent measurements of the differential cross section for these reactions have refined our knowledge of the isospin-dependent part  $U_1$  of the optical potential.<sup>3-6</sup> They also provided quantitative information about the isospin-dependent component  $v_\tau$  of the nucleon-nucleon effective force by comparison with microscopic distorted-wave Born-approximation (DWBA) calculations.<sup>7,8</sup>

In general nuclear reaction cross sections are not very sensitive to spin effects. In the case of QE ( $p, n$ ) reactions, measurements of cross section alone are not sufficient to determine any spin dependence of  $U_1$  and  $v_\tau$ . On the other hand, measurements of the polarization of the outgoing particles or of the analyzing power for reactions induced by polarized projectiles are a natural way of studying such spin effects. As a matter of fact, the first measurements of the analyzing power of QE ( $p, n$ ) reactions<sup>9</sup> gave an indication in favor of a spin dependence of the isospin-dependent part  $U_1$  of the optical potential, in terms of a spin-orbit component  $V_{so}^{(1)}$ . However, due to ambiguities in the optical model, more precise data are required in order to draw quantitative conclusions about the magnitude of  $V_{so}^{(1)}$ . In a similar way the differential cross section for the QE ( $p, n$ ) reactions determines the central part  $v_\tau$  of the isospin-dependent

component of the nucleon-nucleon effective force,<sup>7,8</sup> and we can hope that measurements of the analyzing power give information about the spin-orbit part  $v_{LS\tau}$  of the isospin-dependent effective force. Furthermore, the two interpretations, macroscopic with  $U_1$  and microscopic with  $v_\tau$ , are closely related since, using the reformulated optical model of Greenlees *et al.*,<sup>10</sup>  $U_1$  simply results from a folding between  $v_\tau$  and the neutron excess density distribution.

In order to obtain significant information about  $v_{LS\tau}$  and the spin dependence of  $U_1$  we have performed extensive measurements of the differential analyzing power of QE ( $p, n$ ) reactions induced by 22.8 MeV polarized protons on the nine targets  $^{49}\text{Ti}$ ,  $^{56}\text{Fe}$ ,  $^{64}\text{Ni}$ ,  $^{70}\text{Zn}$ ,  $^{90}\text{Zr}$ ,  $^{96}\text{Zr}$ ,  $^{117}\text{Sn}$ ,  $^{165}\text{Ho}$ , and  $^{208}\text{Pb}$ . The angular range was 15–100°, reduced to forward angles in the case of  $^{165}\text{Ho}$  and  $^{208}\text{Pb}$ . In this paper we give first some details about the experimental techniques used for this measurement. Then we analyze our data from both macroscopic and microscopic points of view. The macroscopic analysis leads to an evaluation of the spin-orbit component  $V_{so}^{(1)}$  of the isospin-dependent part  $U_1$  of the optical potential. However, considerable ambiguities remain in the microscopic analysis, which prevent us from drawing quantitative conclusions about the spin-orbit component  $v_{LS\tau}$  of the isospin-dependent nucleon-nucleon effective interaction.

### II. EXPERIMENT

Our measurements of the analyzing power in QE ( $p, n$ ) reactions were performed at the Saclay

variable energy cyclotron using the polarized proton beam extracted from the cyclotron after external ionization and trochoidal injection.<sup>11</sup> The beam polarization is switched from up to down five times per second. The analyzing power, defined in accordance with the Madison convention, is equal to  $A = (1/P)(N_+ - N_-)/(N_+ + N_-)$ . Here  $P$  is the polarization of the incident beam (around 80%);  $N_+(N_-)$  is the number of events recorded when the beam is polarized with spin up (down); the up direction for the polarization refers to  $\vec{k}_{in} \times \vec{k}_{out}$  where  $\vec{k}_{in}$  ( $\vec{k}_{out}$ ) stands for the momentum of the incident (outgoing) particles.

The new time-of-flight (TOF) neutron spectrometer setup for this experiment allowed an overall resolution less than 2 ns [full width at half maxi-

mum (FWHM)], corresponding to an energy resolution of 400 keV for 11 MeV neutrons and a 5 m flight path. The time structure of the beam (5 ns FWHM) was improved to 1–1.5 ns by slightly detuning the cyclotron from the peak of resonance. The beam intensity on target was then from 1 to 10 nA.

#### A. Beam line

The experimental area is shown schematically in Fig. 1. After extraction from the cyclotron, the beam is brought to focus in the scattering chamber by two pairs of magnetic quadrupoles and is then stopped by a thick graphite plate used as a Faraday cup. In order to reduce the background, the beam

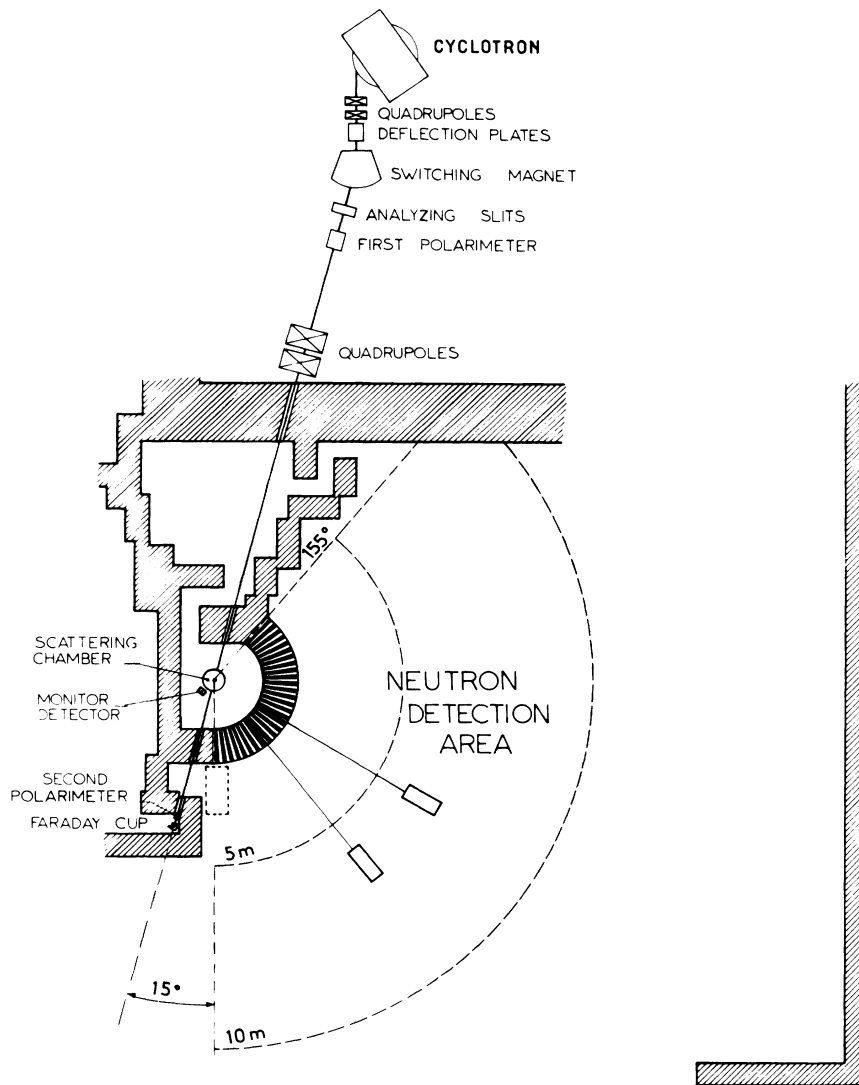


FIG. 1. Schematic layout of the experimental area.

pipe has a big (15 cm) diameter after the second pair of quadrupoles and the scattering chamber is surrounded by concrete walls, at least 60 cm thick, except in the horizontal reaction plane where the shielding is made with 1 m of steel at 1 m from the target. In this shielding there are ports every  $5^\circ$  from  $15^\circ$  to  $155^\circ$ , through which the reaction products reach the detector. During a run these ports, except those located at the two counting angles are walled up with paraffin cast in light steel containers. The Faraday cup is shielded with 20 cm of lead and 60 cm of concrete.

The scattering chamber is simply a hollow Lucite cylinder, 30 cm in diameter, with 2.6 cm thick walls reduced to a thickness of 2 mm in the reaction plane on the side of the neutron detection area. A monitor detector located outside the chamber just behind a Mylar window gives the time of arrival of the protons elastically scattered by the target, and therefore, the time structure of the beam. The monitor is made of a plastic scintillator, 1 cm thick and 0.5 cm in diameter, coupled to a 56 DVP photomultiplier mounted on an Ortec 269 base.

Two polarimeters are shown in Fig. 1. The first

one, placed in front of the target, consists of an aluminum degrader, a thick graphite target ( $61 \text{ mg/cm}^2$ ), and two silicon solid-state detectors at  $55^\circ$  on each side of the beam. This polarimeter measured the absolute polarization of the incident beam after degrading it to a mean energy of 15 MeV where the analyzing power of the  $^{12}\text{C}(p,p)$  reaction is known to be equal to  $-0.75$  at  $55^\circ$  in the laboratory.<sup>12</sup> Measuring the polarization with this polarimeter could only be intermittent since it requires a degradation of the beam energy. Due to the length of our measurements (1 to 10 h) we also needed a continuous polarization monitoring which was achieved by the second polarimeter. This polarimeter was located between the target and the Faraday cup and consisted of a polythene target,  $200 \mu\text{m}$  thick and 5 mm wide, viewed by two silicon solid-state detectors at a variable angle ( $45\text{--}90^\circ$ ). Because of the multiple scattering along the beam pipe from the scattering chamber to the second polarimeter and of the absence of any slit to define the beam in the polarimeter, its efficiency depended upon the nature and thickness of the target used in the experiment. This efficiency was easily calibrated before each target change by

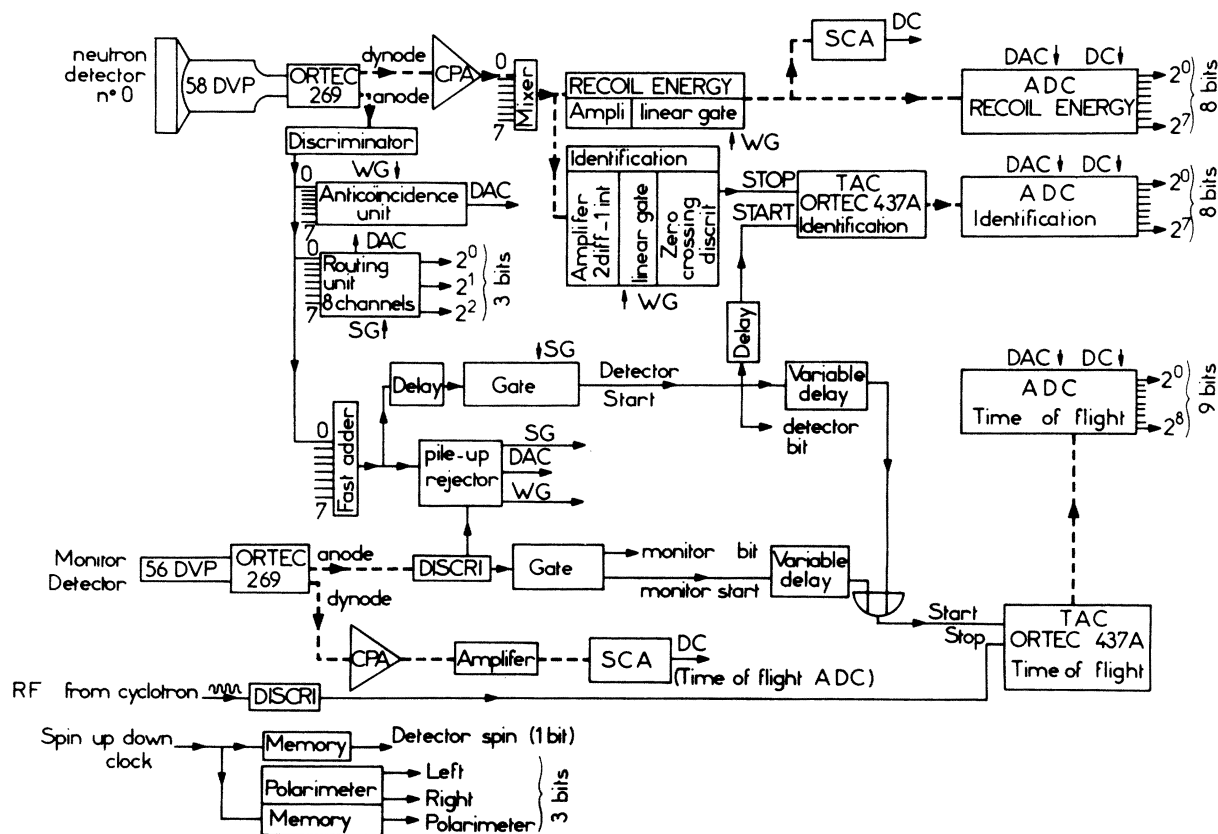


FIG. 2. The electronics setup used in the present experiment.

comparing the measurements obtained with both polarimeters.

### B. Neutron detectors

The small intensity of the beam was compensated by the use of eight large detectors, piled up four by four on two wagons, which made it possible to measure the analyzing power at two angles simultaneously. The wagons mounted on wheels, can be moved easily in the neutron detection area, where the angles from 15 to 155° and the distances between 5 and 10 m are marked. Each detector consists of a 5 cm thick and 20 cm diam container of NE 213 liquid scintillator. It is coupled by a Lucite cone to the photocathode (10 cm useful diameter) of a 58 DVP photomultiplier mounted on an Ortec 269 base. The scintillator container is metallic and is electrically connected to the photocathode by a metallic cone surrounding the light funnel. This connection insures that there cannot be any large potential gradient at the surface of the photomultiplier. A layer of PVC electrical tape insulates the entire detector and provides a light tight wrapping. An outer layer of aluminum foil, grounded at the tube base, provides rf shielding and protects personnel from the high voltage. Finally, magnetic shielding against the earth's field is provided by three layers of Co-Netic foil wrapped around the detector package.

### C. Electronics and data acquisition

The electronics setup used for our analyzing power measurements is shown in Fig. 2. Because of the small intensity of the beam, the counting rate was sufficiently small that it was reasonable to use a single electronics system for the eight neutron detectors. The signals given by the eight detectors are mixed after the charge preamplifiers for the dynode signals and after the leading-edge discriminators for the anode signals. But the discriminators output signals feed a routing unit which codes the number of the detector in which each event occurs. The electronics system provides three kinds of data for each event: the time of flight, the recoil energy, and the identification, using the excellent pulse-shape-discrimination (PSD) properties of NE 213<sup>13</sup> and the standard zero-crossing technique.<sup>14</sup> These data, together with the output of the routing unit and the polarization state of the incident beam, are recorded by an on-line CAE 90-10 computer. With thresholds on the recoil energy and identification spectra depending upon the number of the detector, the treatment of the data becomes equivalent to having one complete system for each detector. The quality of the  $n$ - $\gamma$  discrimination, very important

for this kind of experiment is thus preserved. We finally get for each detector one recoil energy spectrum, one identification spectrum, one  $\gamma$  TOF spectrum, and two neutron TOF spectra corresponding to both polarization states of the incident beam. These spectra are stored in an additional Honeywell ICM-40 memory (16 000 16-bit locations). The  $\gamma$  rays from the target are used to center the TOF spectra and to add them four by four at each angle.

The neutron detectors were calibrated by using the <sup>60</sup>Co  $\gamma$ -ray Compton edge together with published NE 213 response curves,<sup>16</sup> in order to determine for each experiment the threshold on the recoil proton energy. Since we were only interested in the analog-state neutron group, this threshold was always set high enough to prevent TOF overlap, due to the periodicity of the cyclotron beam, between this analog-state neutron group and lower energy neutrons. This solution to the TOF overlap problem was preferred to the usual one that consists of increasing the period of the beam to a convenient value, a procedure which decreases the beam intensity.

The time structure of the beam, measured with the monitor detector, is provided by the same time-to-amplitude converter (TAC) as the neutron TOF. It is also recorded by the computer and the neutron detectors TOF spectra are automatically corrected for possible drifts of the beam time structure. Moreover, the acquisition code periodically calculates its FWHM and stops the run when this FWHM becomes too large compared with a threshold value chosen at the beginning of the experiment. In this case a better time structure of the beam must be looked for by adjusting some shim coils of the cyclotron to insure that data cannot be taken with poor time structure.

Finally, events occurring in the polarimeter detectors are also recorded by the computer in order to monitor continuously the beam polarization. In the same way as for the monitor detector, the acquisition code periodically calculates the instantaneous polarization of the incident beam and stops the run when this polarization becomes too small compared with a threshold value fixed at the beginning of the experiment. This is very important since, if the beam polarization is divided by two, the counting time must be multiplied by four to obtain a given statistical error on the analyzing power. Usually the polarization of the incident beam was around 0.8 and the threshold was fixed at 0.75.

### D. Results

Since we were primarily interested in the analyzing power, the energy and the targets were

TABLE I. List of the targets used in the present experiment.

Isotopes	Z	N	T	$J^\pi$	$Q^a$ (MeV)	$E_x^b$ (MeV)	Thickness (mg/cm <sup>2</sup> )	Thickness (keV)	Enrichment (%)
<sup>49</sup> Ti	22	27	$\frac{5}{2}$	$\frac{7}{2}$	-7.75	5.36	5.0	90	75.7
<sup>56</sup> Fe	26	30	2	0 <sup>+</sup>	-8.87	3.51	8.5	148	91.7
<sup>64</sup> Ni	28	36	4	0 <sup>+</sup>	-9.16	6.70	10.0	166	97.9
<sup>70</sup> Zn	30	40	5	0 <sup>+</sup>	-9.56	8.12	10.0	161	...
<sup>90</sup> Zr	40	50	5	0 <sup>+</sup>	-11.92	5.03	9.9	147	97.6
<sup>96</sup> Zr	40	56	8	0 <sup>+</sup>	-11.64	11.07	9.7	140	72.5
<sup>117</sup> Sn	50	67	$\frac{17}{2}$	$\frac{9}{2}^+$	-13.78	11.18	8.0	109	78.8
<sup>165</sup> Ho	67	98	$\frac{31}{2}$	$\frac{7}{2}^+$	-16.64	15.49	~25	303	100
<sup>208</sup> Pb	82	126	22	0 <sup>+</sup>	-18.98	15.33	10.4	114	99.1

<sup>a</sup> Quasielastic ( $p, n$ ) reaction  $Q$  value, calculated with the formula (Ref. 17):  $Q = -1.444 (Z + 0.5)/A^{1/3} + 1.13$ .

<sup>b</sup> Excitation energy of the analog state in the residual nucleus.

chosen in such a way that absolute cross section measurements are available,<sup>15</sup> except in the case of <sup>70</sup>Zn. For this case we used the Boulder cross section data<sup>15</sup> obtained for <sup>64</sup>Zn and multiplied, according to the predictions of the Lane model<sup>2</sup> for an isotope series, by the ratio of the neutron excesses, here equal to 2.5. To extract only relative cross sections we did not need to measure the efficiency of our neutron detectors.

Another criterion for the choice of the targets was the high excitation energy of the analog states in the residual nucleus, so that the analog state appears over an unpolarized continuum of ( $T_0 - 1$ ) states instead of being located among a small number of levels. This criterion, in general, corresponds to choosing the higher mass isotopes, which is also interesting because the cross section is predicted by the Lane model<sup>2</sup> to be proportional

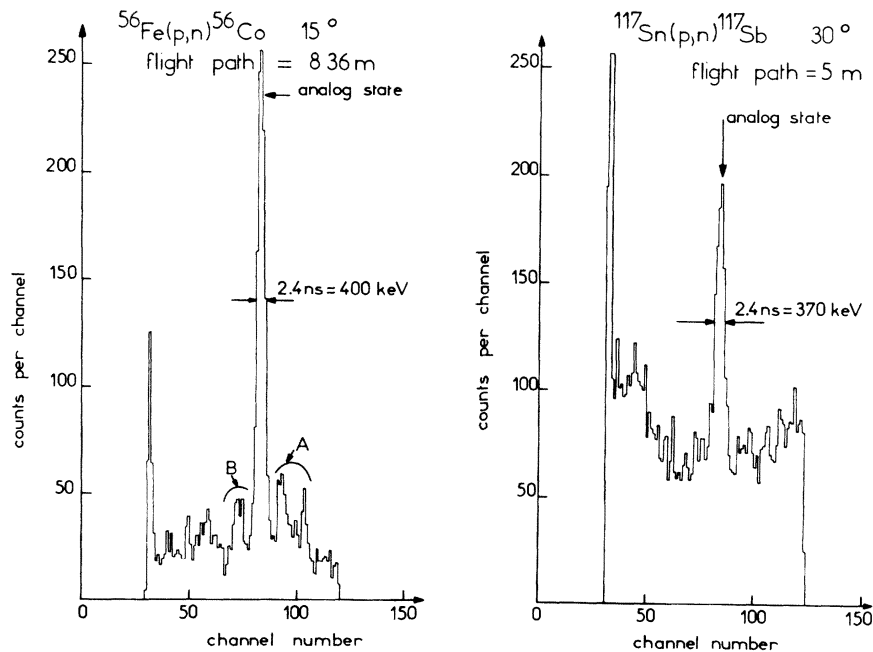


FIG. 3. Typical neutron time-of-flight spectra for the reactions <sup>56</sup>Fe( $p, n$ )<sup>56</sup>Co and <sup>117</sup>Sn( $p, n$ )<sup>117</sup>Sb at 22.8 MeV incident proton energy. The peak at the left of each spectrum is inherent to the working of the time-to-amplitude converter.

to the neutron excess. Moreover, because of the small intensity of the beam, we used relatively thick (around 10 mg/cm<sup>2</sup>) targets, listed in Table I.

Typical neutron TOF spectra, shown in Fig. 3, have been obtained with <sup>56</sup>Fe and <sup>117</sup>Sn targets. The overall resolution, around 2 ns, is sufficient to resolve the analog state. In the case of <sup>117</sup>Sn, which is more typical than <sup>56</sup>Fe, the analog state appears over a continuum of ( $T_0 - 1$ ) states. The background subtraction is quite easy by interpolation between both sides of the analog peak. This background was found to be unpolarized on both sides of the peak and was consequently supposed unpolarized under the analog peak. In the case of <sup>56</sup>Fe, the excitation energy of the analog state in <sup>56</sup>Co is only 3.5 MeV. Instead of appearing over a continuum of ( $T_0 - 1$ ) states, the analog peak is located between unresolved ( $T_0 - 1$ ) states (A) and the 2\* excited analog state (B). The latter is too small to be analyzed. The analog peak is much stronger than the others and can be resolved.

The agreement between our relative cross section measurements and the Boulder absolute measurements<sup>15</sup> is quite satisfactory, except at three forward angles for <sup>96</sup>Zr. Unless otherwise indicated, we shall use for comparison with theoretical calculations the Boulder cross section data,<sup>15</sup> together with our data at the three forward angles for <sup>96</sup>Zr, and our analyzing power data, which are available upon request. Errors indicated in our analyzing power data include only the statistical error. A systematic error due to the uncertainty about the background estimation must be added. It is negligible with respect to the statistical error when the background or the analyzing power is small. However, it becomes comparable with the statistical error when the background and the analyzing power are significantly large. This is clear from the formula  $\Delta A = A(\Delta F/F) F/N$ , where  $A$  and  $\Delta A$  are the analyzing power and its systematic error,  $F$  is the number of counts in the background and  $\Delta F$  its estimated uncertainty, and  $N$  is the number of counts in the peak. Neither the statistical (negligible) nor the systematic (around 5%) error in the determination of the incident beam polarization is included.

### III. MACROSCOPIC LANE-MODEL ANALYSIS

The nucleon-nucleus optical potential can be decomposed, according to the Lane model,<sup>2</sup> into isoscalar and isovector parts:

$$U = U_0 + 4U_1 \vec{t} \cdot \vec{T} / A, \quad (1)$$

where  $\vec{t}$  and  $\vec{T}$  are, respectively, the isospin operators of the nucleon and the nucleus and  $A$  is the

mass of the nucleus. The diagonal elements lead to a dependence of the proton and neutron optical potentials with respect to the nuclear asymmetry  $(N-Z)/A$ . This dependence is well accounted for by global analyses of proton and neutron elastic scattering. The off-diagonal part  $t_+ T_-$  of the potential induces QE transitions between the target ground state  $|T_0 T_0\rangle$  and its analog  $|T_0 T_0 - 1\rangle$  in the residual nucleus. This leads to coupled Schrödinger equations for the  $p$ -target and  $n$ -analog channels. However, since the coupling terms are small, the distorted-wave Born approximation (DWBA) may be used to calculate the transition amplitude of the QE ( $p, n$ ) reactions.<sup>18,19</sup> The equations used are

$$(K + U_0 - 2T_0 U_1 / A + U_C - E_{pT}) \chi_{pT} = 0, \quad (2a)$$

$$[K + U_0 + 2(T_0 - 1)U_1 / A + \Delta_C - E_{pT}] \chi_{nA} = 0, \quad (2b)$$

$$T_{pn} = \langle \chi_{nA} | -2\sqrt{2}T_0 U_1 / A | \chi_{pT} \rangle, \quad (2c)$$

$$(K + U_0 + 2T_0 U_1 / A - E_{nT}) \chi_{nT} = 0, \quad (2d)$$

where  $T_0 = \frac{1}{2}(N - Z)$  is the target isospin,  $K$  is the kinetic energy operator,  $U_C$  is the Coulomb potential,  $\Delta_C$  is the Coulomb displacement energy,  $T_{pn}$  is the transition amplitude for the QE ( $p, n$ ) reaction, and  $\chi_{pT}$ ,  $\chi_{nA}$ ,  $\chi_{nT}$  are the distorted waves describing the  $p$ -target,  $n$ -analog, and  $n$ -target channels respectively.

Therefore the Lane model<sup>2</sup> implies some relations between the  $p$ -target,  $n$ -analog,  $n$ -target, isoscalar, and isovector optical potentials, namely:

$$U_{pT} = U_0 - 2T_0 U_1 / A, \quad (3a)$$

$$U_{nA} = U_0 + 2(T_0 - 1)U_1 / A, \quad (3b)$$

$$U_{nT} = U_0 + 2T_0 U_1 / A, \quad (3c)$$

$$U_0 = \frac{1}{2}(U_{pT} + U_{nT}) = [(T_0 - 1)U_{pT} + T_0 U_{nA}] / (2T_0 - 1), \quad (3d)$$

$$U_1 = (U_{nT} - U_{pT})A / 4T_0 = (U_{nA} - U_{pT})A / (4T_0 - 2) \quad (3e)$$

with the same  $U_0$  and  $U_1$  in the first three equations.

Our DWBA calculations were performed with the program DWUCK.<sup>20</sup> Concerning the inclusion of nonlocality corrections in a DWBA calculation for a QE ( $p, n$ ) reaction, there was recently some controversy between Satchler<sup>21</sup> and Woods.<sup>22</sup> We followed Satchler's point of view and never used such nonlocality corrections. However, it has been found that, unlike the cross section, the analyzing power is rather insensitive to these corrections.

The optical potentials used in our DWBA calculations are of the form

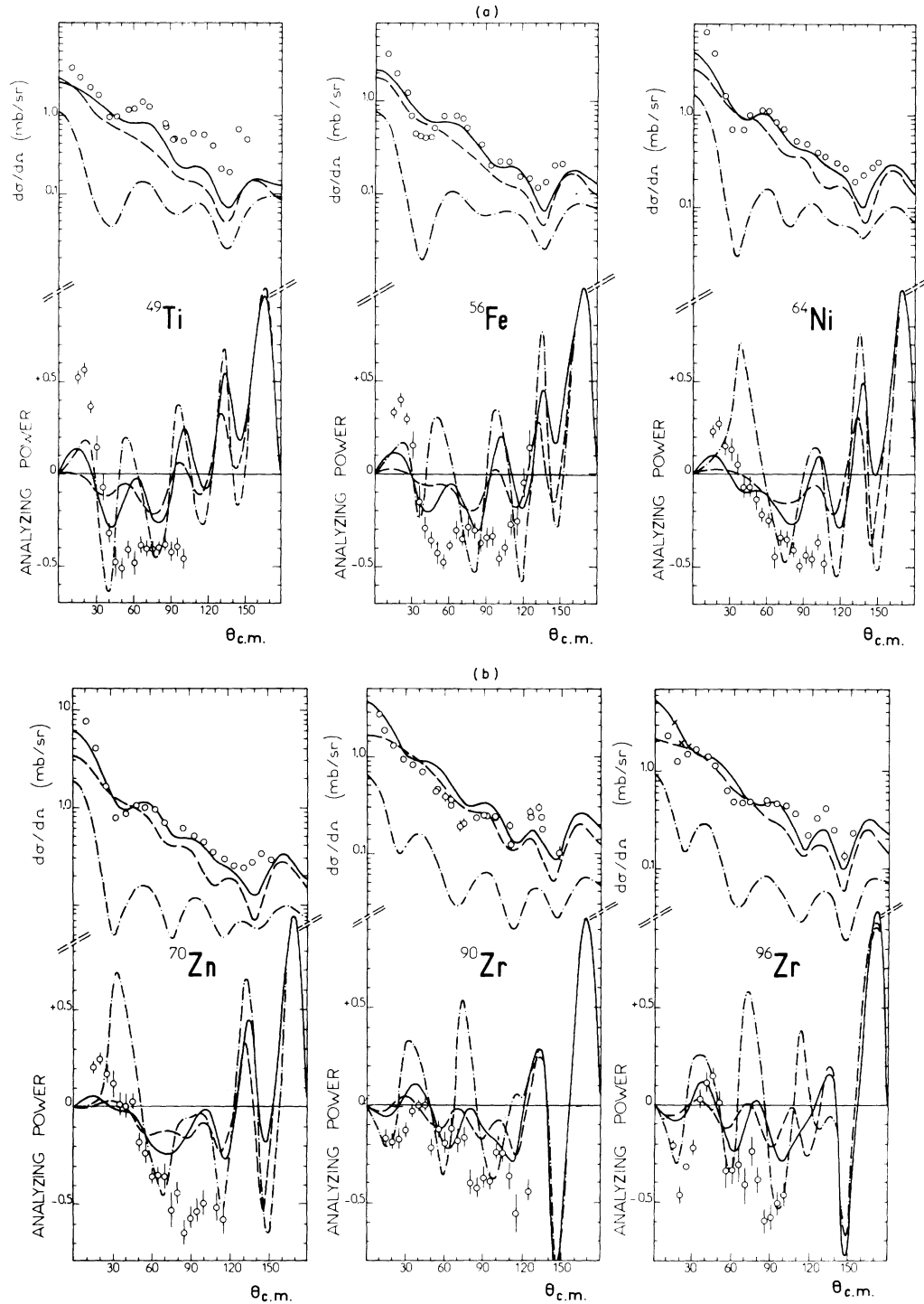


FIG. 4. Differential cross section (Ref. 15) and analyzing power (this work) in QE ( $p, n$ ) reactions at  $E_p = 22.8$  MeV, compared with DWBA predictions using the Becchetti-Greenlees (BG) best-fit optical parameters (Ref. 23), together with the form factor  $U_1$  derived from them, without spin-orbit component  $V_{so}^{\uparrow}$  (solid curves). Dashed (respectively dot-dashed) curves show the contribution of the real volume (respectively imaginary surface) part of the form factor.

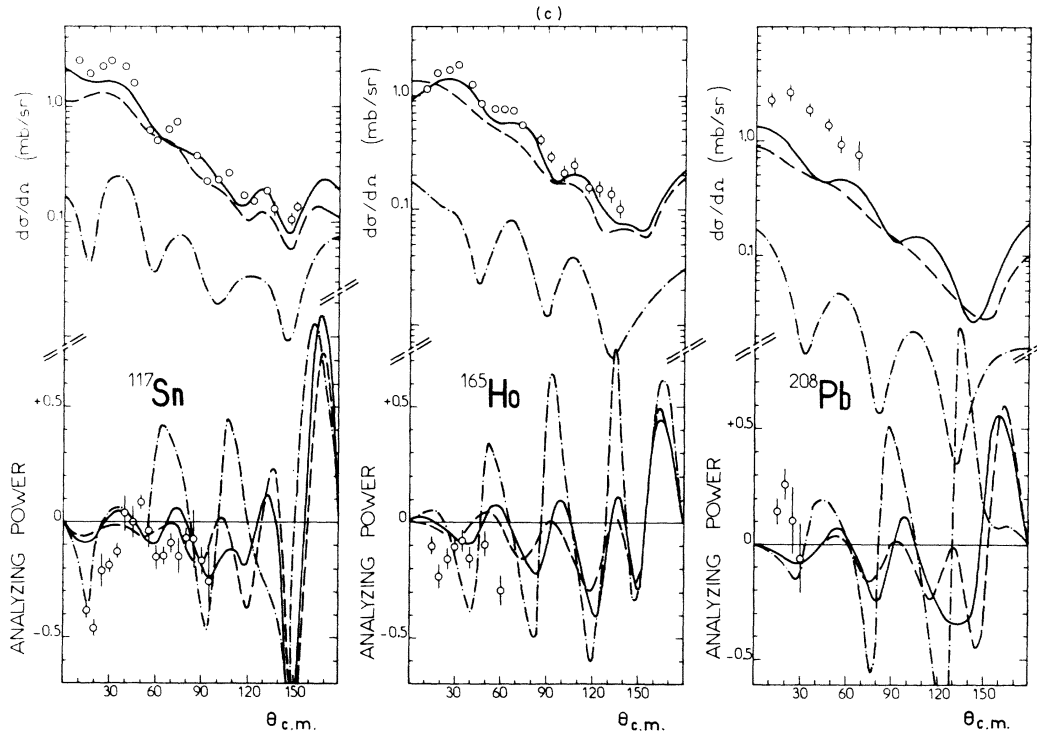


FIG. 4. (Continued)

$$U(r) = -V_R f_R(r) - i[W_v - 4a_I W_{sf}(d/dr)]f_I(r) + V_{so} \vec{\sigma} \cdot \vec{\lambda} r^2 (1/r)(d/dr)f_{so}(r) \quad (4)$$

with Woods-Saxon radial shapes

$$f_i(r) = \{1 + \exp[(r - r_i A^{1/3})/a_i]\}^{-1} \quad (5)$$

for  $i=R, I, so$ . The various kinds of optical potentials used are  $p$  target,  $n$  analog,  $n$  target, isoscalar, and isovector. These potentials will be denoted as subscripts for the total potential  $U$  and as superscripts for each part of the potential: real, imaginary, and spin-orbit. The depths are in MeV and the geometrical parameters (radius and diffuseness) in fm.

#### A. Comparison with predictions based on the Becchetti-Greenlees optical potentials

The Becchetti and Greenlees (BG) "best-fit" optical-model parameters<sup>23</sup> are not entirely consistent within the Lane model,<sup>2</sup> since the proton and neutron optical potentials do not satisfy Eqs. (3a) and (3c) with the same  $U_0$ . However they suggest an isovector part  $U_1$  of the optical potential given by:

$$V_R^{(1)} = -24, \quad r_R = 1.17, \quad a_R = 0.75; \quad (6)$$

$$W_{sf}^{(1)} = -12, \quad r_I = 1.29, \quad a_I = 0.51 + 0.7(2T_0 - 1).$$

The geometrical parameters for the surface imaginary part are the average of the corresponding proton and neutron parameters.

These parameters, i.e. the BG best-fit parameters for the  $p$ -target and  $n$ -analog distorted waves together with the potential  $U_1$  of Eqs. (6) for the form factor, were used as a starting point in our macroscopic analysis. In Fig. 4 the experimental data are compared with DWBA calculations using these parameters and with individual contributions from the volume real and surface imaginary parts  $V_R^{(1)}$  and  $W_{sf}^{(1)}$  of the form factor. In agreement with other calculations,<sup>3-5</sup> the cross section is shown to have the right order of magnitude. But the calculated cross sections present less structure than the experimental ones. This structure is especially given by the surface imaginary part  $W_{sf}^{(1)}$  of the form factor and the agreement can be improved by increasing the ratio  $W_{sf}^{(1)}/V_R^{(1)}$ .<sup>3,5</sup>

As for the analyzing power, the agreement between calculations and experimental data is not very good. The sign of the first extremum at  $20^\circ$  is reproduced, positive for medium mass nuclei ( $^{49}\text{Ti}$ ,  $^{56}\text{Fe}$ ,  $^{64}\text{Ni}$ , and  $^{70}\text{Zn}$ ) and negative for heavier nuclei ( $^{90}\text{Zr}$ ,  $^{96}\text{Zr}$ ,  $^{117}\text{Sn}$ , and  $^{165}\text{Ho}$ ). For  $^{208}\text{Pb}$  the positive sign of this extremum is not given by the calculations, but the experimental points are not very precise and the energy of the exit neutrons is too weak (3.8 MeV) to neglect the compound-nu-

cleus contribution to the transition amplitude. Thus, results obtained for the QE ( $p, n$ ) reaction on  $^{208}\text{Pb}$  will not be considered further. Even if the sign of the first extremum is obtained, its calculated amplitude is never large enough. Moreover, beyond this extremum, the calculated analyzing power is usually less negative than the experimental one.

### B. Sensitivity to the addition of a spin-orbit form factor $V_{so}^{(1)}$

Equations (3) derived from the Lane model<sup>2</sup> must hold in principle for each part of the potential: real, imaginary, and spin-orbit. Optical-model global analyses of nucleon-nucleus elastic scattering<sup>23</sup> as well as Lane-model analyses of QE ( $p, n$ ) reaction cross sections have used these equations for the real and imaginary parts of the potential.

Previous measurements of the analyzing power in QE ( $p, n$ ) reactions<sup>9</sup> favored a spin-orbit part  $V_{so}^{(1)}$  in the isovector component  $V_1$  of the nucleon-nucleus optical potential. A nonvanishing  $V_{so}^{(1)}$  means, according to Eqs. (3) applied to the spin-orbit part of the optical potential, that  $V_{so}^{(pT)}$  and  $V_{so}^{(nT)}$  are not equal, as they are supposed to be in most of the global analyses of nucleon-nucleus elastic scattering.

Such an isovector spin-orbit part  $V_{so}^{(1)}$  in the optical potential may be evaluated in a simple way. According to the reformulated optical model of Greenlees *et al.*,<sup>10</sup> let us assume equal shapes for proton and neutron densities in the nucleus, and also for the isoscalar and isovector components of

the effective nucleon-nucleon force. The ratio of the isovector and isoscalar components of the optical potential is then equal to the ratio of the isovector and isoscalar components of the effective nucleon-nucleon force. This holds as well for the central parts for the spin-orbit part, leading to

$$V_{so}^{(1)}/V_{so}^{(0)} = v_{LS\tau}/v_{LS} \quad (7)$$

if the effective nucleon-nucleon spin-orbit interaction is written as

$$(v_{LS} + v_{LS\tau} \vec{\tau}_1 \cdot \vec{\tau}_2) g_{LS}(r_{12}) \times [(\vec{r}_1 - \vec{r}_2) \times (\vec{p}_1 - \vec{p}_2) \cdot (\vec{\sigma}_1 + \vec{\sigma}_2)]. \quad (8)$$

The  $v_{LS}$  and  $v_{LS\tau}$  components of the effective nucleon-nucleon spin-orbit interaction are related to its components in the triplet-even and triplet-odd states by the following equations:

$$v_{LS} = \frac{1}{4}(3v_{LS}^{TO} + v_{LS}^{TE}) \quad (9)$$

$$v_{LS\tau} = \frac{1}{4}(v_{LS}^{TO} - v_{LS}^{TE}).$$

It is well known from free nucleon-nucleon scattering that the spin-orbit force acts primarily in the triplet-odd state.<sup>24</sup> If we neglect the triplet-even spin-orbit force, Eqs. (7) and (9) lead to:

$$V_{so}^{(1)}/V_{so}^{(0)} = \frac{1}{3}, \quad (10)$$

which gives  $V_{so}^{(1)} = 2$  MeV with the usual 6 MeV value for  $V_{so}^{(0)}$  obtained from optical-model elastic scattering analyses. It should be noted that the sign of the ratio  $V_{so}^{(1)}/V_{so}^{(0)}$  is positive, which means according to Eqs. (3a) and (3c), that the neutron spin-orbit optical potential  $V_{so}^{(nT)}$  is greater

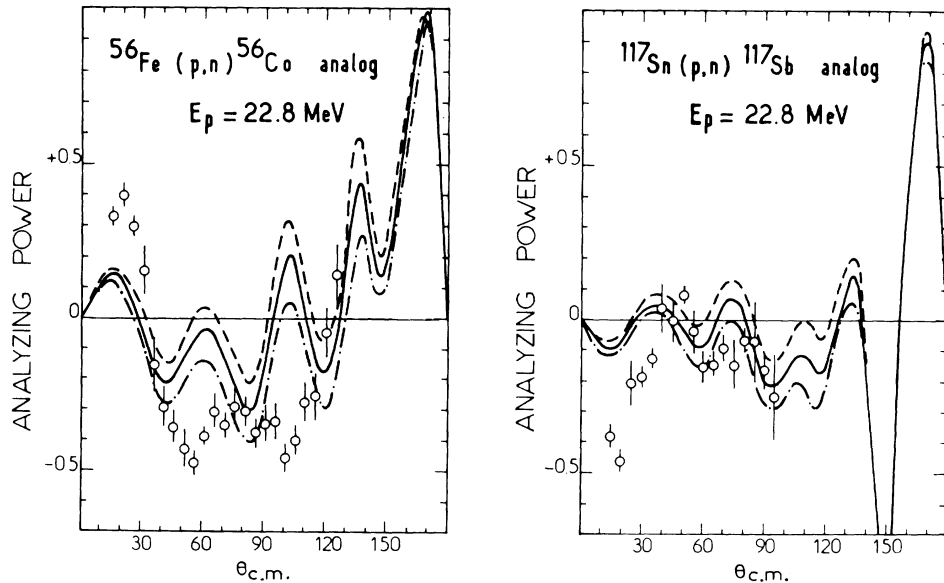


FIG. 5. Effect, on the analyzing power of QE ( $p, n$ ) reactions, of adding a spin-orbit component  $V_{so}^{(1)}$  to the usual central form factor. The curves correspond to  $V_{so}^{(1)} = 0$  (solid),  $V_{so}^{(1)} = -2$  MeV (dashed), and  $V_{so}^{(1)} = 2$  MeV (dot-dashed).

than the proton one  $v_{so}^{(pT)}$ . This result is opposite to that for the volume real central potential  $V_R$ .

In order to study the influence of this isovector spin-orbit part  $V_{so}^{(1)}$  on the QE ( $p, n$ ) reaction analyzing power, a spin-orbit form factor was included in the program DWUCK.<sup>20</sup> In this macroscopic Lane-model analysis the transferred angular momenta, spin  $s$ , orbital  $l$ , and total  $j$ , of a QE ( $p, n$ ) reaction are equal to zero, so that the radial matrix elements  $I_{L_n j_n L_p j_p}^{isj}$  defined by Satchler<sup>25</sup> are diagonal in the orbital ( $L_n = L_p = L$ ) and total ( $J_n = J_p = J$ ) angular momenta of the partial waves in the entrance and exit channels. The radial matrix elements

$$I_{LJ} = \langle \chi_{LJ}^{(-)}(k_n, r) | U_1(r) | \chi_{LJ}^{(+)}(k_p, r) \rangle \quad (11)$$

have to be evaluated with a form factor  $U_1$  given by Eq. (4) and including a spin-orbit part  $V_{so}^{(1)}$ . In this evaluation  $\vec{\sigma} \cdot \vec{l}$  depends on  $L$  and  $J$  and is equal to  $L$  or  $-(L+1)$  according as  $J$  takes the respective values  $L + \frac{1}{2}$  or  $L - \frac{1}{2}$ .

In Fig. 5 is shown the influence of a spin-orbit form factor  $V_{so}^{(1)}$  on the QE ( $p, n$ ) reaction analyzing power for <sup>56</sup>Fe and <sup>117</sup>Sn targets. The optical parameters are the same as in the previous calculation, i.e. the BG best-fit parameters for the distorted waves and the potential  $U_1$  of Eqs. (6) for the form factor, to which has been added a spin-orbit form factor given by

$$V_{so}^{(1)} = \pm 2, \quad r_{so} = 1.01, \quad a_{so} = 0.75.$$

The 2 MeV value for the depth is the simple prediction of Eq. (10) and the geometrical parameters come from the BG best-fit spin-orbit potential. The effect of  $V_{so}^{(1)}$  on the cross section is negligible and not shown. Its effect on the analyzing power is an overall displacement towards negative or positive values according to whether the sign of  $V_{so}^{(1)}$  is positive or negative, respectively, and the greatest displacement takes place at  $90^\circ$ . The agreement with the experimental data is somewhat improved by the addition of a positive  $V_{so}^{(1)}$  predicted by Eq. (10). Moreover it has been found, by using other geometrical parameters for  $V_{so}^{(1)}$  ( $r_{so} = 0.91$  and  $1.11$  with  $a_{so} = 0.75$ ;  $a_{so} = 0.65$  and  $0.85$  with  $r_{so} = 1.01$ ), that the analyzing power is rather insensitive to the particular choice of geometrical parameters for  $V_{so}^{(1)}$ .

This influence of  $V_{so}^{(1)}$  on the QE ( $p, n$ ) reaction analyzing power may be understood in the following way. In this macroscopic Lane model, QE ( $p, n$ ) reactions are  $l = s = j = 0$  transitions. If we further assume a zero spin target nucleus, there only remain two amplitudes  $X$  and  $Y$  corresponding respectively to the conservation and the inversion of the spin projection of the projectile. The analyzing power  $A$  is related to these amplitudes  $X$  and  $Y$  by

$$A = 2 \operatorname{Im}(YX^*) / (|X|^2 + |Y|^2). \quad (12)$$

In the same way as in elastic scattering,  $X$  and  $Y$  may be expressed in a partial wave expansion:

$$X = \sum_{L=0}^{\infty} [(L+1)I_{L^+} + LI_{L^-}] P_L(\cos\theta), \quad (13)$$

$$Y = \sum_{L=1}^{\infty} (I_{L^+} - I_{L^-}) P_L^1(\cos\theta);$$

but instead of being phase shifts, the  $I_{L^+}$  and  $I_{L^-}$  are the radial matrix elements of Eqs. (11). The plus and minus signs stand for the two possible values of  $J$  for a given  $L$ . If the total form factor  $U_1$  includes a spin-orbit part  $V_{so}^{(1)}$ , the  $I_{LJ}$ 's may be separated into  $I_{LJ}^{(C)}$  and  $I_{LJ}^{(so)}$  integrals, respectively, with the central and spin-orbit parts of  $U_1$ , so that:

$$I_{L^+} = I_{L^+}^{(C)} + LI_{L^+}^{(so)} \quad (14)$$

and

$$I_{L^-} = I_{L^-}^{(C)} - (L+1)I_{L^-}^{(so)}.$$

In order to isolate the effect of  $V_{so}^{(1)}$  on the analyzing power, we may assume that there is no spin-orbit distortion in the entrance and exit channels, so that the radial matrix elements do not depend on  $J$ . Then the  $X$  and  $Y$  amplitudes become:

$$X = \sum_{L=0}^{\infty} (2L+1)I_L^{(C)} P_L(\cos\theta) \quad (15)$$

and

$$Y = \sum_{L=1}^{\infty} (2L+1)I_L^{(so)} P_L(\cos\theta)$$

If we neglect the  $|Y|^2$  contribution to the denominator in Eq. (12) with respect to the  $|X|^2$  one, the analyzing power becomes linear in  $I_L^{(so)}$ . Therefore it must depend approximately linearly on the depth of  $V_{so}^{(1)}$ .

### C. Sensitivity to the distorted-wave spin-orbit potentials

*A priori* the analyzing power is also determined to a great extent by the spin-orbit potentials  $V_{so}^{(pT)}$  and  $V_{so}^{(nA)}$  used for the entrance and exit channels. In particular, when  $V_{so}^{(pT)}$  and  $V_{so}^{(nA)}$  are equal to zero,  $V_{so}^{(1)}$  is also equal to zero [Eq. (3e)], and the analyzing power is zero.

In their global optical-model analysis of nucleon-nucleus elastic scattering,<sup>23</sup> Becchetti and Greenlees found a parameter set which differs from their best-fit parameters only in the spin-orbit potentials. More precisely these spin-orbit potentials

are given by:

$$\begin{aligned} V_{so}^{(pT)} &= 5.9, \quad r_{so} = 1.17, \quad a_{so} = 0.60; \\ V_{so}^{(nA)} &= 6.4, \quad r_{so} = 1.17, \quad a_{so} = 0.58. \end{aligned} \quad (16)$$

This parameter set, which we denote as BG Set 2, gives nearly as good agreement as the best-fit parameters to the elastic scattering polarization data. It should be noted that the spin-orbit potential is greater for neutrons than for protons, in agreement with the sign of  $V_{so}^{(1)}$  obtained with the simple model of Sec. III B.

In Fig. 6 are compared with experimental data for  $^{49}\text{Ti}$ ,  $^{56}\text{Fe}$ ,  $^{90}\text{Zr}$ , and  $^{96}\text{Zr}$ , the results of two DWBA calculations using the same form factor  $U_1$  derived from BG best-fit parameters [see Eq. (6)], but the BG best-fit and the BG Set 2 parameters for the distorting potentials. The effect on the cross section of such a change in the spin-orbit potentials is very small and restricted to backward angles; it is not shown. As for the analyzing power, the first extremum at  $20^\circ$  is enhanced by using the BG Set 2 parameters, which improves agreement with experimental data, but beyond this

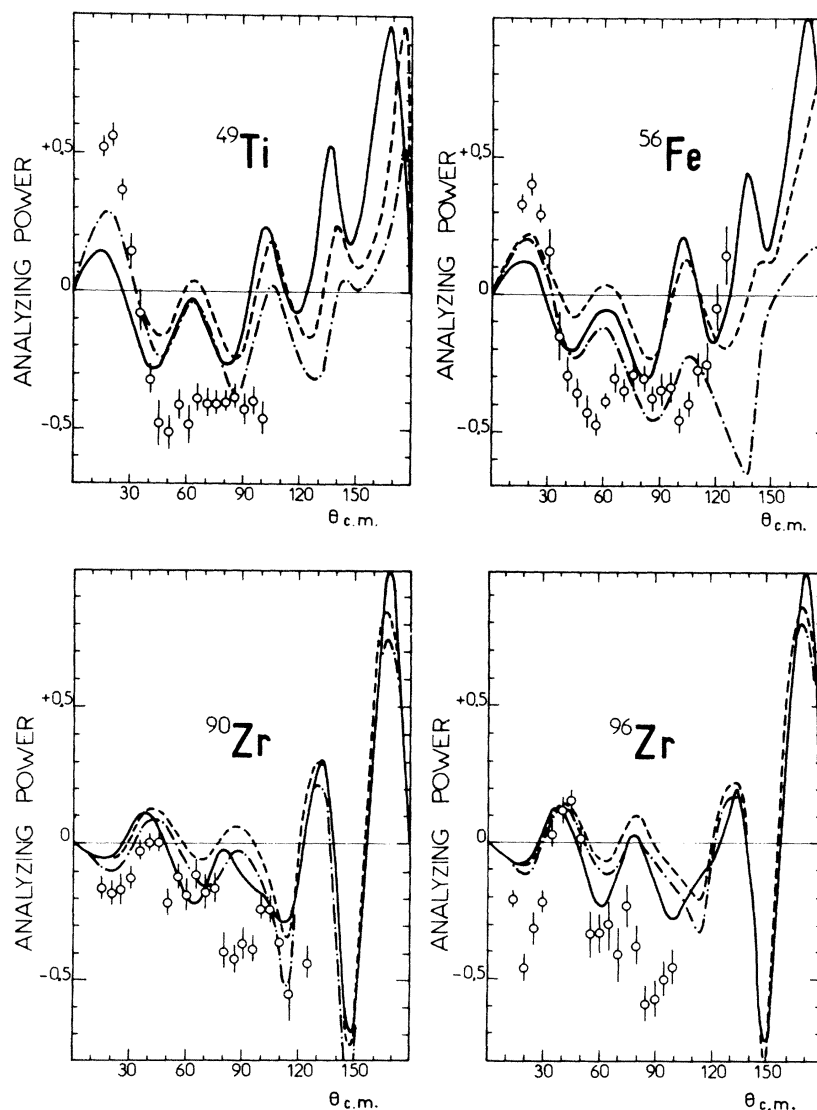


FIG. 6. Differential analyzing power in QE ( $p, n$ ) reactions at  $E_p = 22.8$  MeV, compared to DWBA predictions using optical parameters differing only in the distorted-wave spin-orbit potentials. The solid (respectively dashed) curves correspond to BG best-fit (respectively BG Set 2) optical parameters defined in the text. The dot-dashed curves show the effect of adding a spin-orbit form factor  $V_{so}^{(d)}$  consistent with BG Set 2 parameters.

extremum the analyzing power is displaced towards positive values in disagreement with experimental data.

Since the spin-orbit potentials of BG Set 2 are not equal for proton and neutron channels, they are consistent with a spin-orbit term  $V_{so}^{(1)}$  in the form factor that can be calculated from Eqs. (3):

$$V_{so}^{(1)} = A/(8T_0 - 4), \quad r_{so} = 1.17, \quad a_{so} = 0.59,$$

where the diffuseness  $a_{so}$  is the average of the proton and neutron diffuseness parameters. The results of a DWBA calculation using BG Set 2 parameters and including this consistent  $V_{so}^{(1)}$  form factor are also shown in Fig. 6. In the same way as in Sec. III B, the inclusion of the  $V_{so}^{(1)}$  form factor displaces the analyzing power towards negative values, which now improves the fit to experimental data if compared with the calculation using BG Set 2 parameters without  $V_{so}^{(1)}$ .

Moreover, it has been found that the difference in calculations using BG best-fit and BG Set 2 parameters is primarily due to the difference in the geometrical parameters  $r_{so}$  and  $a_{so}$ . The analyzing power is rather insensitive to small changes in the depths of the proton and neutron spin-orbit potentials.

#### D. Attempt to evaluate the isovector spin-orbit optical potential $V_{so}^{(1)}$

In this section we take advantage of the sensitivity of the QE ( $p, n$ ) reaction analyzing power to the spin-orbit form factor  $V_{so}^{(1)}$  in order to determine  $V_{so}^{(1)}$ . However, as the analyzing power has been found to be very sensitive to the geometrical parameters of the distorted-wave spin-orbit potentials these parameters will be kept fixed in a first step and the geometrical ambiguities will be discussed later on.

On the other hand DWBA calculations in Secs. III B and C showed that the differential cross section for the QE ( $p, n$ ) reactions is rather insensitive to both the spin-orbit form factor  $V_{so}^{(1)}$  and variations in the distorted-wave spin-orbit potentials which maintain the fit to elastic scattering polarization data. To the contrary the cross section depends very much on the relative amount of volume real  $V_R^{(1)}$  and surface imaginary  $W_{sf}^{(1)}$  form factors (see Sec. III A) and can be used to determine it. In order to determine  $V_{so}^{(1)}$  by fitting our analyzing power data, we needed optical parameters fitting both elastic scattering data and QE ( $p, n$ ) reaction cross sections<sup>5</sup> better than the BG best-fit parameters used in Sec. III A. Therefore we have used, as a starting point, the energy-dependent, Lane-model consistent, nucleon-nucleus optical potential of Patterson *et al.*<sup>6</sup> determined by

fitting QE ( $p, n$ ) reaction cross sections between 25 and 45 MeV while maintaining the fit obtained Becchetti and Greenlees<sup>23</sup> to proton elastic scattering data. Patterson *et al.* obtained two equivalent parameter sets, according to the number of parameters in the search. These sets are labeled A and B, and are listed in Table II.

Values for  $V_{so}^{(1)}$  have been determined by using a least-squares search program to fit our analyzing power data. The function subroutine was not the DWBA program DWUCK<sup>20</sup> itself, but its subroutine XSECT somewhat modified in order to calculate cross section and analyzing power after adding with various weights amplitudes already computed by the program DWUCK and stored on a magnetic disk. These amplitudes correspond to calculations involving only the central part of the isovector potential  $U_1$  or its spin-orbit part  $V_{so}^{(1)}$ . This procedure is not entirely consistent within the Lane model since, according to Eq. (3),  $V_{so}^{(nA)}$  must be varied if  $V_{so}^{(1)}$  is varied while keeping  $V_{so}^{(pT)}$  at a fixed value. However, it may be iterated by calculating new transition amplitudes with the  $V_{so}^{(nA)}$  obtained by Eq. (3d) from the  $V_{so}^{(1)}$  results of the search and from  $V_{so}^{(pT)}$ , which is kept fixed in order to maintain the fit to the proton elastic scattering polarization data, then by using these amplitudes in a new search for  $V_{so}^{(1)}$ , and so on. This iteration procedure converges very rapidly, as could be expected from the results of Sec. III C which showed that the analyzing power is rather insensitive to small changes in the depths of  $V_{so}^{(pT)}$  and  $V_{so}^{(nA)}$ . In fact the first iteration was in general accurate enough and only the results of this first iteration will be subsequently shown.

Fitted values of  $V_{so}^{(1)}$ , obtained with the parameter Sets A and B of Patterson *et al.*,<sup>6</sup> are listed in Table III as a function of the target nucleus. This result is rather satisfactory since the  $V_{so}^{(1)}$  values are concentrated around the mean value of 4.3 MeV

TABLE II. The energy-dependent, Lane-model consistent, nucleon-nucleus optical potential of Patterson *et al.* (Ref. 6) used as a starting point to determine  $V_{so}^{(1)}$ . The form of the potential is given by Eqs. (1) and (4).  $E$  is given by:  $E_{pT} = (E_p - \bar{V}_C)$ ,  $E_{nA} = (E_p - \Delta_C)$ ,  $E_{nT} = E_n$ , and  $E_{pn} = \frac{1}{2}(E_{pT} + E_{nA})$  with  $\bar{V}_C = 0.84Z/A^{1/3}$ . All parameters not listed are the same as the  $V_{CC} = 0.84$  proton parameters of Ref. 23.

		$V_R$	$W_{sf}$
Set A	$U_0$	$56.4 - 0.34 E$	$9.2 - 0.20 E$
	$U_1$	$-12.2 - 0.25 E$	$-22.1 + 0.51 E$
Set B	$U_0$	$55.8 - 0.32 E$	$9.6 - 0.22 E$
	$U_1$	$-17.7$	$-18.1 + 0.31 E$

TABLE III. Fitted values of  $V_{so}^{(1)}$ , as a function of the target nucleus and of the parameter set used in the search.

Parameter \ Target	$^{49}\text{Ti}$	$^{56}\text{Fe}$	$^{64}\text{Ni}$	$^{70}\text{Zn}$	$^{90}\text{Zr}$	$^{96}\text{Zr}$	$^{117}\text{Sn}$	$^{165}\text{Ho}$	$^{208}\text{Pb}$	Mean value
A	4.7	5.0	3.6	3.0	3.9	6.2	3.2	5.0	...	4.4
B	4.6	4.8	3.6	3.0	3.5	5.8	2.8	6.5	...	4.3
A2	6.7	6.4	5.3	4.9	6.2	7.9	3.7	5.3	...	5.8
B2	6.4	6.1	5.3	5.3	6.0	8.2	4.2	7.3	...	6.1

which is not inconsistent with the 2 MeV value predicted by the simple model of Sec. III B. Moreover, this mean value is nearly the same for both Sets A and B. Remembering the possible ambiguity due to the geometrical parameters used for the distorted-wave spin-orbit potentials, we have made a search with other parameter sets labeled A2 and B2. These two sets differ from the Sets A and B only in the geometry used for the spin-orbit potential, in a similar way as BG best fit and BG Set 2 differed in Sec. III C, namely:  $r_{so} = 1.17$ ,  $a_{so} = 0.60$ ,  $V_{so}^{(pT)} = 5.9$  for the Sets A2 and B2, instead of  $r_{so} = 1.01$ ,  $a_{so} = 0.75$ ,  $v_{so}^{(pT)} = 6.2$  for the Sets A and B. Fitted values of  $V_{so}^{(1)}$  obtained with the parameter Sets A2 and B2 are also listed in Table III. The result is again satisfactory, since the  $V_{so}^{(1)}$  values are still concentrated around a mean value, now equal to 6 MeV, which is nearly the same for both Sets A2 and B2. This ambiguity in the  $V_{so}^{(1)}$  average values corresponds approximately to a constant product of the depth and the diffuseness, which is reasonable for a surface peaked potential.

To better visualize the improvement due to the spin-orbit form factor  $V_{so}^{(1)}$ , the variation of the  $\chi^2$  per degree of freedom ( $\chi^2/N$ ) obtained for the analyzing power with the parameter Set B2 is plotted in Fig. 7 against the  $V_{so}^{(1)}$  value for each target nucleus. The minimum is very well pronounced, except for the two heavier nuclei  $^{165}\text{Ho}$  and  $^{208}\text{Pb}$ . Finally experimental cross section and analyzing power angular distributions are compared in Fig. 8 with two DWBA calculations, the first one using the parameter Set A without a spin-orbit form factor  $V_{so}^{(1)}$ , the second one using the same parameter Set A to which has been added the 4.3 MeV mean value of  $V_{so}^{(1)}$  resulting from the least-squares search. The addition of the spin-orbit form factor  $V_{so}^{(1)}$  hardly changes the cross section but results in an overall improvement of the fit to the analyzing power data. However, too many qualitative discrepancies remain between theory and experiment. In particular one can see in Fig. 8 that for the medium mass isotopes ( $^{49}\text{Ti}$ ,  $^{56}\text{Fe}$ ,  $^{64}\text{Ni}$ , and  $^{70}\text{Zn}$ ), the first extremum of the analyzing power keeps the right sign, positive, but is not enhanced towards experimental values. For

these isotopes the improvement is obtained beyond this first extremum, especially for  $^{64}\text{Ni}$  and  $^{70}\text{Zn}$ , but if the average amplitude of the analyzing power is there reproduced, its phase is not, and for  $^{56}\text{Fe}$  there is even a phase opposition between experiment and theory. For  $^{90}\text{Zr}$  and  $^{96}\text{Zr}$  the improvement of the fit is clearer. For the three heavier nuclei ( $^{117}\text{Sn}$ ,  $^{165}\text{Ho}$ , and  $^{208}\text{Pb}$ ) the predictions do not differ enough to provide discrimination between  $V_{so}^{(1)}$  equal to and different from zero. This can also be seen on the  $\chi^2/N$  curves (Fig. 7) which are rather flat for these isotopes. At this point should be recalled the remark about the possible compound nucleus contribution for  $^{208}\text{Pb}$  (see Sec. III A). For  $^{165}\text{Ho}$  the analyzing power data are also rather poor and the Lane-model analysis with a spherical potential is not very well suited for this deformed nucleus.

One possible reason for these discrepancies could be the momentum mismatch due to the large  $Q$  value of the QE ( $p, n$ ) reactions compared to the 22.8 MeV incident energy, in contrast to inelastic scattering to low lying excited states. On the other

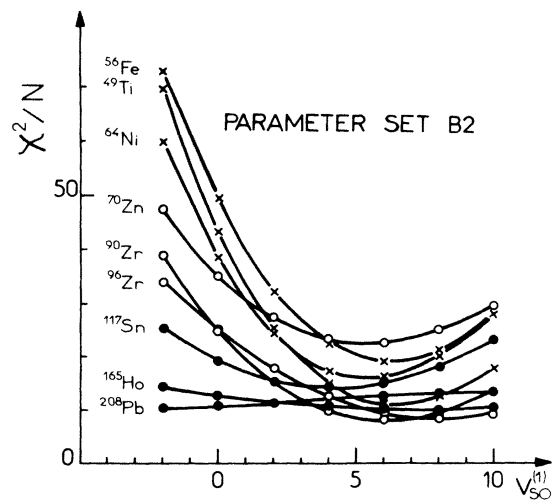


FIG. 7. Variation of the  $\chi^2$  per degree of freedom obtained for the analyzing power with the parameter Set B2, plotted against the depth of the spin-orbit form factor  $V_{so}^{(1)}$  for each target nucleus.

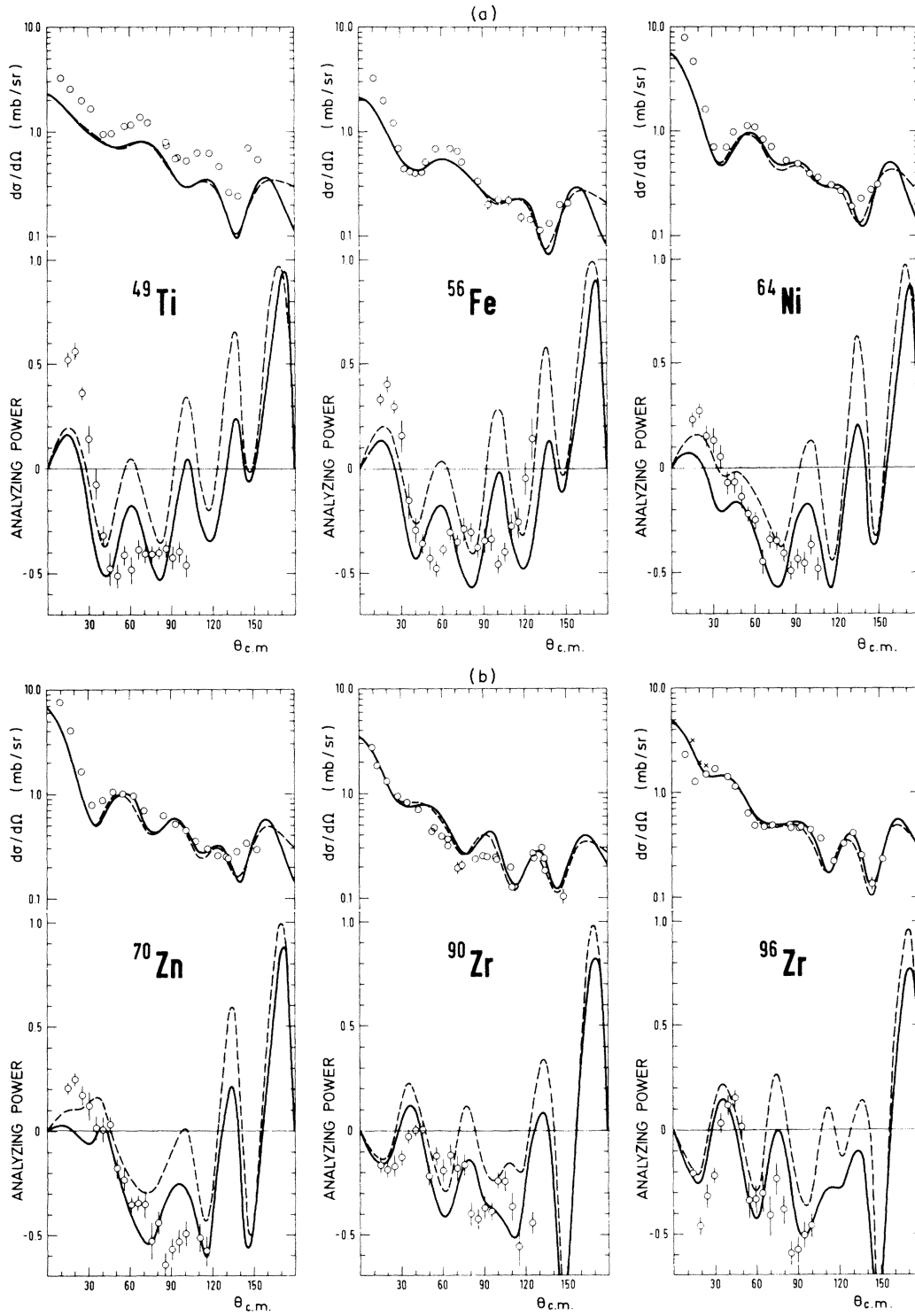


FIG. 8. Differential cross section (Ref. 15) and analyzing power (this work) in QE ( $p, n$ ) reactions at  $E_p = 22.8$  MeV, compared to DWBA predictions using the parameter Set A (see Table II) without a spin-orbit form factor  $V_{so}^{(1)}$  (dashed curve) and with the 4.3 MeV mean value of  $V_{so}^{(1)}$  resulting from a least-squares search (solid curve).

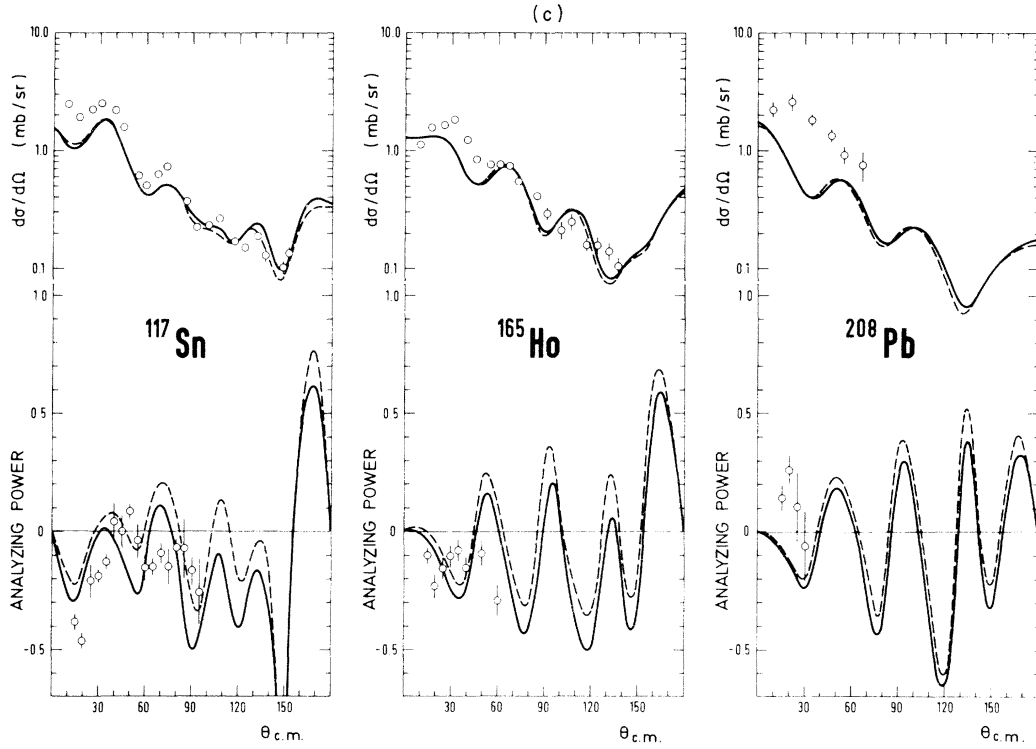


FIG. 8. (Continued)

hand, it should be noted that the 4.3 MeV value for  $V_{so}^{(1)}$  is only a mean value, and the agreement would be somewhat better if the best-fit value of  $V_{so}^{(1)}$  were used for each target nucleus. With the parameter Set B instead of Set A, the results look very much the same. With the parameter Set A2 and B2, the  $\chi^2$  is a little smaller than with Sets A and B but the qualitative discrepancies already obtained with Set A (or B) are rather bigger, in that the first extremum becomes negative for  $^{64}\text{Ni}$  and  $^{70}\text{Zn}$ , and the oscillations of the analyzing power are even larger than with Set A (or B).

#### IV. MICROSCOPIC DWBA ANALYSIS

In the distorted-wave theory of direct nuclear reactions,<sup>25</sup> the transition amplitude for the QE ( $p, n$ ) reaction can be written:

$$v_{ip} = [v_0(r_{ip}) + v_\tau(r_{ip}) \vec{\tau}_i \cdot \vec{\tau}_p] + [v_\sigma(r_{ip}) + v_{\sigma\tau}(r_{ip}) \vec{\tau}_i \cdot \vec{\tau}_p] \vec{\sigma}_i \cdot \vec{\sigma}_p + [v_{LS}(r_{ip}) + V_{LS\tau}(r_{ip}) \vec{\tau}_i \cdot \vec{\tau}_p] \vec{L} \cdot \vec{S} + [v_T(r_{ip}) + v_{T\tau}(r_{ip}) \vec{\tau}_i \cdot \vec{\tau}_p] S_{12} \quad (18)$$

including spin-orbit ( $\vec{L} \cdot \vec{S}$ ) and tensor ( $S_{12}$ ) interactions. If the exchange term due to the antisymmetrization between the projectile nucleon and the bound nucleons in the target is not taken into ac-

$$T_{pn}(\vec{k}_p, \vec{k}_n) = \int \chi_{nA}^{(-)*}(\vec{k}_n, \vec{r}_n) \langle nA | V | pT \rangle \chi_{pT}^{(+)}(\vec{k}_p, \vec{r}_p) d\vec{r}_p d\vec{r}_n, \quad (17)$$

where  $V$  is the interaction responsible for the transition. In the macroscopic Lane-model analysis  $\langle nA | V | pT \rangle$  was the isovector part of the one-body nucleon-nucleus optical potential, which led to the amplitude (2c). The microscopic approach<sup>26,27</sup> lies in calculating the nuclear matrix element  $\langle nA | V | pT \rangle$  in terms of the effective interaction between individual nucleons. The target- $T$  and analog- $A$  wave functions are put into individual nucleon wave functions and related by spectroscopic amplitudes. The interaction  $V$  is the sum,  $V = \sum_i v_{ip}$ , of the effective interactions between the free projectile and the individual bound nucleons in the target. The effective interaction  $v_{ip}$  is usually decomposed as

count, only the  $\vec{\tau}_i \cdot \vec{\tau}_p$  terms in  $v_{ip}$  can contribute to the QE ( $p, n$ ) reaction amplitude [Eq. (17)]. Moreover, if the target is an even-even spherical nucleus, the  $\vec{\sigma}_i \cdot \vec{\sigma}_p$  and  $S_{12}$  terms do not contribute.

Only  $v_\tau$  and  $v_{LS\tau}$  remain and can give a contribution to the amplitude. In the case of QE ( $p, n$ ) reactions the spectroscopic amplitudes are simply related, within the shell model, to the neutron excess numbers in each shell. This neutron excess is rather well known, so that QE ( $p, n$ ) reactions are expected to give quantitative information about the  $v_\sigma$  and  $V_{LS\tau}$  components of the nucleon-nucleon effective force. Cross sections for the QE ( $p, n$ ) reactions have already been used to get the  $v_\tau$  component, the more recent work being Ref. 8; on the other hand analyzing power data, *a priori* much more sensitive to spin effects than the cross section, should give information about the  $v_{LS\tau}$  component. Of course a microscopic calculation has to include antisymmetrization effects but we could expect that the effect of  $v_{LS\tau}$  yet remains predominant on the analyzing power.

The antisymmetrized DWBA calculations have been performed with the program DWBA 70 (Ref. 27) which uses the helicity representation.<sup>28</sup> The analysis has been restricted to four  $0^+$  target nuclei, namely  $^{56}\text{Fe}$ ,  $^{64}\text{Ni}$ ,  $^{90}\text{Zr}$ , and  $^{96}\text{Zr}$ . The  $^{64}\text{Ni}$  ground state has been represented by a wave function based on average occupation probabilities derived from a BCS model of  $^{63}\text{Ni}$  and  $^{65}\text{Ni}$  (Ref. 29). Elementary shell-model configurations have been assumed for the other targets, namely  $(1f_{7/2})^2(2p_{3/2})^2$ ,  $0.8(1g_{9/2})^{10} + 0.6(1g_{9/2})^8(2p_{1/2})^2$ , and  $(1g_{9/2})^{10}(2d_{5/2})^6$  for the excess neutrons in  $^{56}\text{Fe}$ ,  $^{90}\text{Zr}$ , and  $^{96}\text{Zr}$ , respectively. The single-particle wave functions have been calculated in a potential of the form (4) without an imaginary part and with  $\vec{l} \cdot \vec{\sigma} = j(j+1) - l(l+1) - s(s+1)$ ;  $r_R = r_{so} = 1.25$ ;  $a_R = a_{so} = 0.65$ ;  $V_{so} = 6$ ;  $l$ ,  $s$ , and  $j$  are the orbital, spin, and total angular momentum quantum numbers, respectively, of the bound nucleon, and  $V_R$  has been adjusted to reproduce its binding energy. The neutron binding energies have been calculated from the empirical formula in Ref. 30. The differences between the binding energies of neutrons and protons in "analog" orbits have been taken to be QE ( $p, n$ ) reaction  $Q$  values (see Table I). The unbound protons are treated by DWBA 70 as bound by 0.01 MeV.

Experimental cross sections and analyzing powers are compared in Fig. 9 (solid curves) to antisymmetrized DWBA calculations using the parameter Set B (see Table II) for the entrance and exit channel distorting potentials, together with a realistic force,<sup>30</sup> derived from the  $G$ -matrix elements of the Reid potential<sup>31</sup> in an oscillator basis (central and tensor-even interactions), and from the effective oscillator  $G$ -matrix elements given by Elliot *et al.*<sup>32</sup> (tensor-odd and spin-orbit interaction). This realistic force is expressed, for compatibility with DWBA 70, as a superposition of Yukawa po-

tentials listed in Table IV. Only the even terms have been retained in the central force, since the central interaction in odd states appears to be much weaker.<sup>33</sup> The  $v_\tau$  component of this realistic

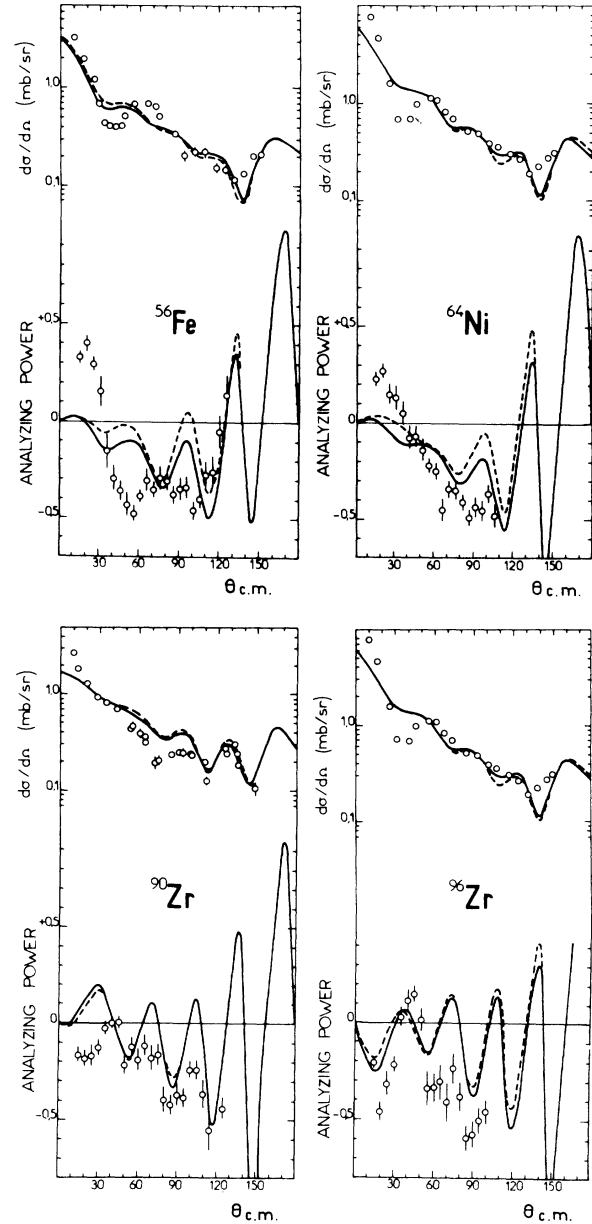


FIG. 9. Differential cross section (Ref. 15) and analyzing power (this work) in QE ( $p, n$ ) reactions at  $E_p = 22.8$  MeV, compared to microscopic antisymmetrized DWBA calculations using the optical parameter Set B (see Table II) for the distorted-wave and the realistic nucleon-nucleon effective interaction of Ref. 30 (see also Table IV). The solid curves are for the entire interaction and the dashed curves for the interaction without its spin-orbit part.

TABLE IV. Nucleon-nucleon effective interaction (Ref. 30) used for calculations shown in Fig. 9. Each component (single-even central. . .) is a superposition of Yukawa potentials, the depths and ranges of which are listed in this table.

Range (fm)	Central		Depth (MeV) Tensor		Spin-orbit	
	Singlet even	Triplet even	Even	Odd	Even	Odd
0.2	5294.5	12 040.9	-28 717.7	3884.4	-2033.4	-26 803.7
0.4	3007.8	2776.3	537.0	-245.6	-643.4	-195.6
0.5	-2419.2	-3012.9	-421.4	210.5	103.8	38.9
0.7			-28.3			

force is comparable with the value of  $v_r$  determined by fitting QE ( $p, n$ ) reaction cross sections.<sup>8</sup> The right order of magnitude is obtained for the cross section, as it has been shown by Doering *et al.*,<sup>8</sup> but the experimental cross section presents more structure than the calculated one, especially for <sup>56</sup>Fe and <sup>64</sup>Ni where the first minimum is completely missed by the calculation. As for the analyzing power, there is no quantitative agreement between theory and experiment. The first extremum is not obtained by the theory, except for <sup>96</sup>Zr, but the phase of the oscillations is approximately reproduced, except for <sup>56</sup>Fe.

In Fig. 9 the spin-orbit part of the nucleon-nucleon interaction is switched on and off. In this procedure the calculated cross sections are hardly changed by the spin-orbit term. The <sup>56</sup>Fe and <sup>64</sup>Ni analyzing powers are slightly shifted towards negative values, an effect which is similar to that of  $V_{so}^{(1)}$  in the macroscopic analysis. For <sup>90</sup>Zr and <sup>96</sup>Zr the spin-orbit term has a very small effect on the calculated analyzing power. It looks then unrealistic to draw quantitative conclusions about the spin-orbit effective interaction from QE ( $p, n$ ) reaction analyzing power data.

The situation is even worse for the  $v_{LS\tau}$  component. As a matter of fact, in order to unravel the effect of  $v_{LS\tau}$ , it was switched off alone. The effect is so small that it would be undistinguishable in the figure. Therefore the  $v_{LS}$  component which acts through the exchange term, turns out to be

much more important than  $v_{LS\tau}$ . Actually this result is in agreement with Eq. (9) since we use (Table IV) a nearly purely odd spin-orbit force and in that case  $v_{LS\tau} \sim \frac{1}{3}v_{LS}$ .

Since the two-step ( $p, d$ )( $d, n$ ) process has proven to be important with respect to the direct charge exchange mechanism,<sup>7</sup> we have done calculations which include this process by using the coupled channels program CHUCK.<sup>34</sup> The fit to the shape of the cross section is then improved and the analyzing power is considerably modified. However, this procedure adds too many parameters to the microscopic calculations to allow any conclusion.

Anyway, even if very good fits were achieved with a good knowledge of the reaction mechanism and of the optical potentials, no information on  $v_{LS\tau}$  would be provided from our QE ( $p, n$ ) analyzing power data since the inclusion of  $v_{LS\tau}$  produces very little effect on the calculated analyzing powers, an effect of smaller magnitude than the experimental error bars.

#### ACKNOWLEDGMENTS

The authors wish to thank the technical staff of the Saclay cyclotron for their help in running the experiments. They are indebted to J. Thirion for his support of the project. Finally they are grateful to Professor J. Blair for critical comments and reading of the manuscript and to J. Raynal and R. Schaeffer for helpful discussions.

<sup>1</sup>G. R. Satchler, in *Isospin in Nuclear Physics*, edited by D. H. Wilkinson (North-Holland, Amsterdam, 1969).

<sup>2</sup>A. M. Lane, *Phys. Rev. Lett.* **8**, 171 (1962); *Nucl. Phys.* **35**, 676 (1962).

<sup>3</sup>C. Wong *et al.*, *Phys. Rev. C* **5**, 158 (1972).

<sup>4</sup>J. D. Carlson, D. A. Lind, and C. D. Zafiratos, *Phys. Rev. Lett.* **30**, 99 (1973); *Nucl. Phys.* **A249**, 29 (1975).

<sup>5</sup>R. K. Jolly, T. M. Amos, A. Golonsky, R. Hinrichs,

and R. St. Onge, *Phys. Rev. C* **7**, 1903 (1973).

<sup>6</sup>D. M. Patterson, R. R. Doering, and A. Galonsky, *Nucl. Phys.* **A263**, 261 (1976).

<sup>7</sup>L. D. Rickertsen and P. D. Kunz, *Phys. Lett.* **47B**, 11 (1973).

<sup>8</sup>R. R. Doering, D. M. Patterson, and A. Galonsky, *Phys. Rev. C* **12**, 378 (1975).

<sup>9</sup>J. M. Moss, C. Brassard, R. Vyse, and J. Gosset,

- Phys. Rev. C 6, 1698 (1972).
- <sup>10</sup>G. W. Greenlees, G. J. Pyle, and Y. C. Tang, Phys. Rev. 171, 1115 (1968); C. J. Batty, E. Friedman, and G. W. Greenlees, Nucl. Phys. A127, 368 (1969).
- <sup>11</sup>R. Beurtey and J. M. Durand, Nucl. Instrum. Methods 57, 313 (1967).
- <sup>12</sup>P. Schnabel, thèse Docteur-Ingenieur, Orsay, 1971 (unpublished).
- <sup>13</sup>R. A. Winyard, J. E. Lutkin, and G. W. McBeth, Nucl. Instrum. Methods 95, 141 (1971).
- <sup>14</sup>K. Alexander and F. Goulding, Nucl. Instrum. Methods 13, 244 (1961).
- <sup>15</sup>R. F. Bentley, J. D. Carlson, D. A. Lind, R. B. Perkins, and C. D. Zafiratos, Phys. Rev. Lett. 27, 1081 (1971).
- <sup>16</sup>D. L. Smith, R. G. Polk, and T. G. Miller, Nucl. Instrum. Methods 64, 157 (1968).
- <sup>17</sup>J. D. Anderson, C. Wong, and J. W. McClure, Phys. Rev. 138, B615 (1965).
- <sup>18</sup>E. M. Schwarcz, Phys. Rev. 149, 752 (1966).
- <sup>19</sup>G. R. Satchler, R. M. Drisko, and R. H. Bassel, Phys. Rev. 136, B118 (1964).
- <sup>20</sup>P. D. Kunz, Univ. of Colorado (unpublished).
- <sup>21</sup>G. R. Satchler, Phys. Lett. 44B, 13 (1973).
- <sup>22</sup>T. J. Woods, Phys. Lett. 46B, 41 (1973).
- <sup>23</sup>F. D. Becchetti and G. W. Greenlees, Phys. Rev. 182, 1190 (1969).
- <sup>24</sup>T. Hamada and I. D. Johnston, Nucl. Phys. 34, 382 (1962).
- <sup>25</sup>G. R. Satchler, Nucl. Phys. 55, 1 (1964).
- <sup>26</sup>G. R. Satchler, Nucl. Phys. A95, 1 (1967).
- <sup>27</sup>R. Schaeffer, Ph.D. thesis, Paris, 1969 (unpublished).
- <sup>28</sup>J. Raynal, Nucl. Phys. A97, 572 (1967).
- <sup>29</sup>V. Gillet, R. Giraud, and M. Rho, Nucl. Phys. A103, 257 (1967).
- <sup>30</sup>J. Borysowicz, H. Mc. Manus, and G. Bertsch, Michigan State University Cyclotron Laboratory Report, 1974 (unpublished).
- <sup>31</sup>R. Reid, Ann. Phys. (N.Y.) 50, 411 (1968).
- <sup>32</sup>J. P. Elliot *et al.*, Nucl. Phys. A121, 241 (1968).
- <sup>33</sup>W. G. Love and G. R. Satchler, Nucl. Phys. A159, 1 (1970).
- <sup>34</sup>E. Rost (private communication).